International Journal of Pharmaceutics 694 (2026) 126727

Contents lists available at ScienceDirect

International Journal of Pharmaceutics

journal homepage: www.elsevier.com/locate/ijpharm

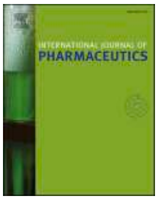

Microfluidic production of silk fibroin nanoparticles: Process optimization and modeling

Edoardo Bertania [a,1], Angelo Modena [a,1], Alessandro Caimi [b], Marco Bellotti [b], Luca Romizi [b], Maurizio Rinaldi [a], Ivana Miletto [a], Elia Bari [a,*], Lorena Segale [a], Giada Diana [a], Alessandro Candiani [a], Maria Luisa Torre [a,c], Ferdinando Auricchio [b]

[a] *University of Piemonte Orientale, Department of Pharmaceutical Sciences, Largo Donegani 2, 28100 Novara, Italy*
[b] *University of Pavia, Department of Civil Engineering and Architecture, Via Ferrata 3, 27100 Pavia, Italy*
[c] *PharmaExceed S.r.l, Piazza Castello 19, 27100 Pavia, Italy*

ARTICLE INFO

Keywords:
Silk fibroin nanoparticles
Microfluidic nanoprecipitation
Computational fluid dynamics
Predictive modeling
Process optimization

ABSTRACT

Silk fibroin is an attractive material for drug delivery due to its biocompatibility, stability, and ability to form nanoparticles through solvent-induced self-assembly. Although microfluidic nanoprecipitation offers superior control and reproducibility compared to batch methods, its rational optimization remains challenging because the tight coupling between flow dynamics, solvent exchange, and fibroin self-assembly hinders nanoparticle formation. Here, we present an integrated experimental-computational framework that combines Design of Experiments, machine-learning prediction, and computational fluid dynamics (CFD) to investigate how operating conditions influence the formation of silk fibroin nanoparticles (SFNs) within a specific microfluidic geometry. The combined effects of fibroin:acetone ratio (1:3–1:5) and total flow rate (8–140 mL/min) were systematically investigated, with particle size and distribution quantified by Nanoparticle Tracking Analysis. Linear, power-law, and Random Forest models captured non-linear interactions between operating parameters, identifying intermediate to high flow rates and higher acetone fractions as optimal for producing small, homogeneous nanoparticles. CFD simulations mechanistically rationalize these trends by quantifying mixing efficiency, shear rate, residence time, and solvent-rich regions that trigger fibroin nanoprecipitation. CFD-derived descriptors, including Volume of Change and process efficiency, delineated parameter regions associated with controlled desolvation and uniform nanoparticle formation. By integrating experimental data, data-driven modeling, and CFD-based mechanistic analysis, this study demonstrates how these complementary approaches can elucidate structure-process relationships in microfluidic SFN production. While the insights are system-specific, the proposed workflow provides a transparent and mechanistically grounded approach for interrogating complex nanoprecipitation processes and informing hypothesis-driven process refinement in related microfluidic systems.

1. Introduction

Silk fibroin has emerged as a promising biopolymer for the development of drug delivery systems owing to its excellent biocompatibility, biodegradability, mechanical robustness, and ease of functionalization (Wani et al., 2022, Yadav et al., 2024). Derived from the cocoons of *Bombyx mori*, fibroin mainly exists in two conformations – Silk I (water-soluble) and Silk II (water-insoluble) – enabling solvent-triggered conformational transitions and self-assembly into nanostructures under appropriate physicochemical conditions (Kong, 2021, Pacheco et al., 2022). When processed into nanoparticles, silk fibroin offers tunable size, controllable degradation rate, and the capacity to encapsulate both hydrophilic and hydrophobic therapeutic molecules (Sánchez-Trasviña et al., 2024, Lammel et al., 2010, Bayraktar et al., 2023), making silk fibroin nanoparticles (SFNs) attractive carriers for the controlled and targeted drug delivery (Pham and Tiyaboonchai, 2020, Bari et al., 2023).

Several fabrication strategies for SFNs have been developed, including desolvation, salting-out, and electrospraying (Zhao et al., 2015, Bari et al., 2020). However, conventional batch processes often

---

* Corresponding author.
E-mail address: elia.bari@uniupo.it (E. Bari).
[1] These authors contributed equally.

https://doi.org/10.1016/j.ijpharm.2026.126727
Received 10 December 2025; Received in revised form 25 February 2026; Accepted 26 February 2026

suffer from poor reproducibility, limited scalability, and significant batch-to-batch variability (Matthew et al., 2022b, Matthew et al., 2020). In addition, desolvation typically requires large volumes of organic solvents, raising environmental and toxicological concerns (Roblin et al., 2023). Microfluidic technologies have therefore gained increasing attention as a more controllable and sustainable alternative for nanoparticle synthesis (Matthew et al., 2022a, Ferrera et al., 2024). By manipulating fluid streams within microscale channels, microfluidics enables precise control over mixing, nucleation, and particle growth, resulting in narrower size distributions, improved reproducibility, and reduced solvent consumption compared to batch methods (Matthew et al., 2022a, Mansor et al., 2025). Several studies have demonstrated the feasibility of microfluidic SFN production, primarily by empirically correlating flow rate, solvent ratio, or mixer geometry with particle size and morphology. For example, Wongpinyochit et al. reported tunable SFN sizes by adjusting flow rate and solvent ratio (Wongpinyochit et al., 2019), while Solomun et al. highlighted improved homogeneity and reproducibility relative to manual fabrication, alongside the influence of fibroin stock properties on final particle characteristics (Solomun et al., 2020); Matthew et al. provided early mechanistic insights into the role of flow-induced mixing and shear on SFN self-assembly (Matthew et al., 2022a). More recently, Ferrera et al. demonstrated GMP-like microfluidic SFN production, emphasizing the translational potential of this approach (Ferrera et al., 2024), and scalability studies confirmed that microfluidic nanoprecipitation can be scaled without compromising nanoparticle quality (Mansor et al., 2025).

Despite these advances, most microfluidic studies rely primarily on empirical optimization and lack predictive frameworks capable of capturing non-linear parameter interactions or explaining batch-to-batch variability from first principles. In particular, the absence of integrated data-driven modeling and fluid-dynamic analysis limits the rational definition of operating windows that are both scalable and mechanistically robust. As a result, reported optimal conditions are often system-specific and difficult to generalize. Integrating machine-learning approaches with computational fluid dynamics (CFD) offers a powerful strategy to overcome these limitations by directly linking experimental outcomes to the hydrodynamic and transport phenomena governing the Silk I → Silk II transition during nanoprecipitation (Zhao et al., 2015).

In this context, the present work introduces a hybrid experimental-computational framework that combines Design of Experiments (DOE), data-driven modeling, and CFD simulations to support mechanistically informed analysis and parameter exploration of microfluidic SFN production. SFNs were produced by acetone-induced nanoprecipitation while systematically varying the fibroin:acetone volumetric ratio and the total flow rate. Particle size and homogeneity were quantified experimentally, while CFD simulations were used to characterize mixing efficiency, local shear rate, residence time, and solvent-rich regions responsible for triggering fibroin desolvation. Quadratic power-law and Random Forest models were developed to capture non-linear parameter interactions and identify experimentally favourable operating regions within the explored design space. Rather than introducing a new nanoparticle formulation, this study establishes a mechanistically interpretable, transferable workflow that links operating parameters to SFN size distribution and homogeneity through physically meaningful descriptors such as shear rate, solvent exposure, and residence time, integrating experimental observations with CFD-derived transport phenomena to enable structured process understanding and reproducible microfluidic SFN manufacturing.

2. Materials and methods

2.1. Materials

Bombyx mori cocoons were kindly donated by Nembri Industrie Tessili, Capriolo, Italy. Sodium carbonate (Na_2CO_3) and lithium bromide (LiBr) were purchased from Merck, Milan, Italy. Acetone was purchased from Carlo Erba Reagenti, Milan, Italy. The dialysis membranes and easySTRAINER filters were purchased from VWR International, Milan, Italy. Microfluidic consumables were purchased from Microfluidic ChipShop, Jena, Germany.

2.2. Silk fibroin extraction and solubilization

Silk fibroin was extracted from the cocoons of *Bombyx mori*. The cocoons were cut into small pieces and washed under running water to remove any residues. The degumming process was performed with a boiling 0.02 M aqueous solution of Na_2CO_3, to which the cocoons were added and left to boil for 30 min. Subsequently, the degummed fibres were washed in distilled water to remove salt and sericin residues; this washing operation was repeated three times, with the water changed each time. After the last wash, the fibroin was left to dry at room temperature.

Once completely dry, the fibroin was solubilized using an aqueous solution of LiBr (100% w/v) and then placed in a thermostatic bath at 65 °C for 4 h. The obtained solution was transferred into a dialysis membrane (3.5 kDa cut-off) and incubated in distilled water for 72 h at room temperature. Subsequently, the solubilized fibroin was filtered through an easySTRAINER (70 μm) to remove any remaining solid residues. The final concentration of fibroin was then calculated gravimetrically after complete solvent (water) evaporation, ranging from 5 to 7% w/v.

2.3. Preparation of silk fibroin nanoparticles

SFNs were prepared using an in-house microfluidic device, further described in section 2.6. The machine consists of two syringe pumps connected to a commercial microfluidic chip (Fluidic 640 from Darwin Microfluidics) – selected after an initial screening of different geometries (data not shown) – with the geometry pictured in Fig. 1.

Specifically, the first syringe contains acetone, while the second contains fibroin diluted to 1.5% w/v (Pirota et al., 2023, Bari et al., 2021). Acetone is injected into the chip through the inlet indicated by the red arrow in Fig. 1, surrounding the fibroin, which enters from the second syringe at the point indicated by the green arrow. The flows in the microfluidic chip are thus continuous: acetone forms a continuous phase around the fibroin stream. Unlike droplet-based or segmented flows, the fibroin and acetone streams interact in a co-flow single-phase regime, ensuring controlled desolvation and exposure times critical to producing homogeneous nanoparticles. The two pumps deliver a precise volume of each corresponding reagent at a precise speed, according to the fibroin:acetone ratios and total flow rate set in the in-house

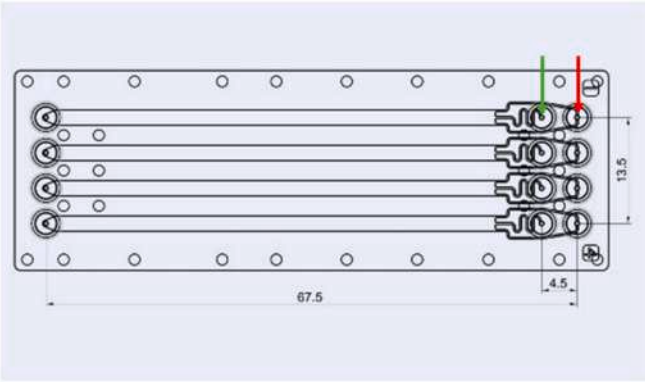

Fig. 1. Geometry of the microfluidic chip Fluidic 640. Each microfluidic chip contains four channels, all with the same geometric layout. The red arrow indicates the injection point for acetone, while the green arrow indicates the injection point for fibroin.

developed software (Blink, Version: 2.27.34, 03.05.2022 12:07:00). For the different batch preparations, experimental conditions were systematically varied according to a DOE, as reported in Table 1, with two levels for the fibroin:acetone ratio and six levels for the total flow rate, which is the combined flow rate of both pumps.

The fibroin:acetone ratio is defined as a volumetric ratio and as a flow rate ratio between the two pumps. Preliminary experiments at 1:1 and 1:2 fibroin:acetone ratios were performed; as nanoparticle formation did not occur under these conditions, consistent with our previous work (Ferrera et al., 2024), these ratios were excluded from further investigations. According to each condition, three batches of SFNs were prepared. Once prepared, SFNs were transferred into a dialysis membrane (3.5 kDa cut-off) and incubated in distilled water for 72 h at room temperature to eliminate acetone residues.

2.4. *Characterization of silk fibroin nanoparticles*

2.4.1. *Nanoparticle Tracking analysis*

SFN size distribution was analyzed using Nanoparticle Tracking Analysis (NTA) technology with the NanoSight NS300 equipment (Malvern Instruments, Malvern, United Kingdom), which analyzes video footage to track the Brownian motion of individual nanoparticles illuminated by a laser beam and calculates their size using the Stokes-Einstein equation. Fresh samples of SFNs were diluted (1:10 or 1:100), sonicated for 30 min in an ultrasound bath on ice to break up aggregates, and then analyzed. For each batch, five 60-second measurements were performed, and the raw data were exported to an Excel file for further analysis.

2.4.2. *Scanning electron microscopy*

SFNs were freeze-dried at a pressure of 8×10^{-1} mbar, and a temperature of −50 °C for 72 h (Modulyo® Edwards Freeze dryer, Kingston, United States of America), and their morphology was then investigated by Field Emission Scanning Electron Microscopy (SEM; GeminiSEM-360, Carl Zeiss S.p.A., Milan, Italy). Samples were observed as dried, previously Pt-sputter-coated (4 nm thick Pt layer) powders under argon. The samples were imaged at 1 kV acceleration voltages, using the InLens SE detector and working distances of 1.5 to 2.0 mm.

2.5. *Modeling and interpretation of operating conditions within the experimental domain*

Raw particle size data were processed and analyzed using the software R (R: The R poject for Statistical computing). From each experimental particle size distribution curve, the deciles (d_{10}-d_{100}) and the mode were extracted. The total flow rate and flow ratio were considered experimental factors. The objective was to identify the conditions that resulted in the smallest mean particle size and the lowest dispersion. Linear models were first fitted to evaluate the influence of experimental factors on particle size and homogeneity. Specifically, to assess particle homogeneity, the difference d_{80}-d_{20} was used, while particle size was investigated using the median (d_{50}) and the mode. Additionally, power and Random Forest models were developed to capture non-linear relationships and to interpret the effects of experimental conditions within the studied domain. In detail, a Random Forest regression model was trained with the caret package (Kuhn, 2008) using the train function with method = "rf" and k-fold cross-validation; the mtry parameter was selected, and the fitted model was then used to predict response surfaces as a function of flow ratio and total flow rate. Model robustness was assessed through the k-fold cross-validated prediction performance, which is a standard approach for ensemble learning methods.

Table 1
Experimental conditions used to prepare the batches.

Ratio	Total flow rate (mL/min)
1:3	8.0
1:3	21.5
1:3	35.0
1:3	70.0
1:3	105.0
1:3	140.0
1:5	8.0
1:5	21.5
1:5	35.0
1:5	70.0
1:5	105.0
1:5	140.0

2.6. *Computational fluid dynamics simulations*

To further enhance the impact of experimental fluid-dynamic conditions on mixing and SFN production, CFD simulations were performed. The fluid domain of one channel of the microfluidic chip shown in Fig. 1 was recreated in ANSYS Discovery, using the geometrical characteristics reported in Fig. 2D. A symmetry condition on the mid xz-plane was adopted to reduce the final number of elements and the relative computational cost. Moreover, the length of the inlets was reduced to 5 times the hydraulic diameter to allow a complete development of the flow profile before entering the main mixing section.

The numerical domain was then discretized using a structured hexahedral computational grid with a characteristic dimension of 10 μm. The boundary conditions to be simulated were derived from experimental conditions that yielded promising results. In detail, using proper total flow rate and flow rate ratio, the velocities were calculated and superimposed on the cross-section of the chip's three inlets. The specific values are reported in Table 2 for a fibroin:acetone ratio of 1:3 and 1:5.

A third and fourth set of numerical simulations were conducted using the values obtained from the Random Forest model and selected based on numerical evidence, respectively (Table 3).

The fluids used to simulate the mixing process, acetone and a fibroin water solution (1.5% w/v), were characterized using a Kinexus Plus Rheometer (Malvern Panalytical, Malvern, United Kingdom): acetone, a classical Newtonian fluid, exhibited constant viscosity as expected, whereas the fibroin-water solution showed clear shear-thinning, or pseudoplastic, behavior, with viscosity decreasing as shear rate increased, as the macromolecular protein fibroin unravels and aligns with the flow at increasing shear rate (Fig. S1). Despite the process being isothermal, and the mass diffusion coefficient (i.e., Dm) being considered negligible at such high flow rates, the adopted model required the imposition of a value, and the classical interdiffusion coefficient for water was considered. Therefore, the rheological properties used in the CFD simulation are reported in Table 4; for the fibroin solution, a non-Newtonian shear-dependent Power Law was adopted (Pinho et al., 2003), with the consistency index (*k*) and power-law index *(n)* determined from the fitting of the experimental rheological curve.

A dimensionless analysis of the flow regimes is reported in the supplementary materials section (File F4). All the obtained numerical data were post-processed to define parameters related to the two fluidic variables involved in SFN formation: shear rate and water:acetone ratio within a specified control volume. The calculation of the acetone/water ratio is fundamental for the desolvation of the protein and its transition from the Silk I to the Silk II conformation, both of which are necessary for the formation of nanoparticles. As a first step, the regions within the microfluidic chip where fibroin is sufficiently exposed to the desolvating agent were identified. According to the literature, effective desolvation requires acetone concentrations above 70% (Ferrera et al., 2024). Using this criterion, the control volumes in which the mass fractions of fibroin and acetone fall within the desired range were extracted, representing the optimal environment for SFN formation. This parameter was defined as the Volume of Change (VoC) and calculated as follows (Bellotti et al., 2024, Giglio et al., 2024):

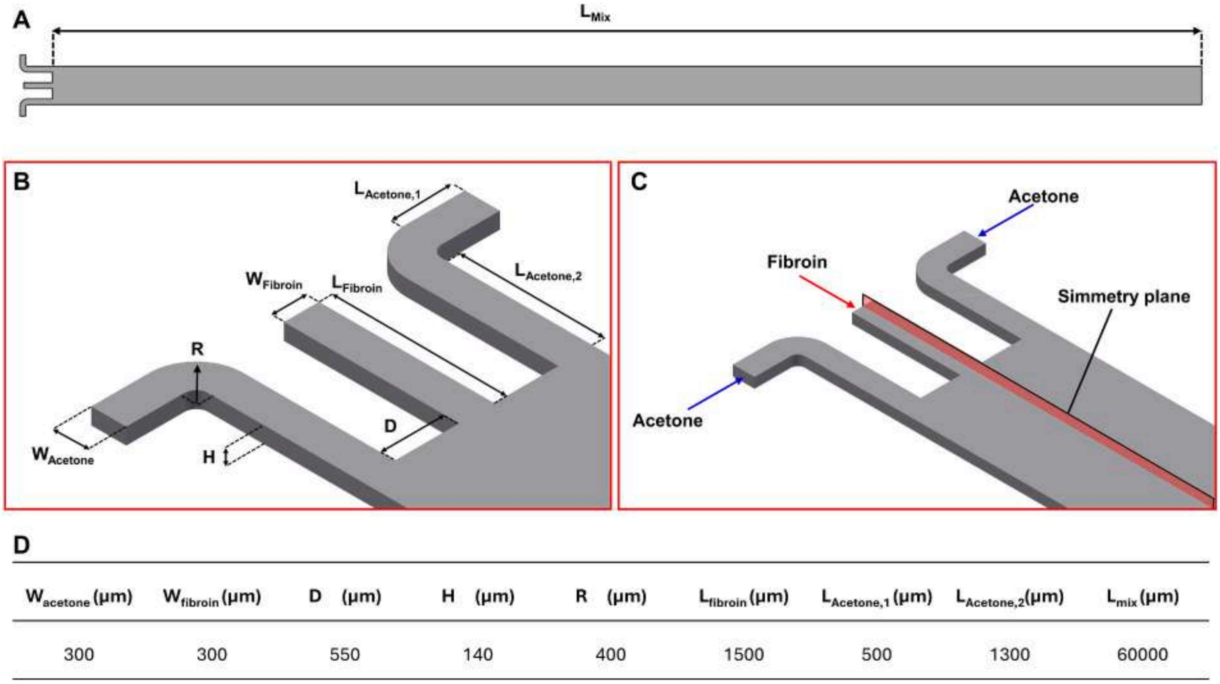

$W_{acetone}$ (μm)	$W_{fibroin}$ (μm)	D (μm)	H (μm)	R (μm)	$L_{fibroin}$ (μm)	$L_{Acetone,1}$ (μm)	$L_{Acetone,2}$ (μm)	L_{mix} (μm)
300	300	550	140	400	1500	500	1300	60000

Fig. 2. (**A**) Fluid domain of the microfluidic chip Fluidic 640. (**B**) Magnification of the inlets with their dimensions (values in μm are reported in **D**). (**C**) An aqueous fibroin solution is injected in the middle channel (red arrow), and acetone for desolvation is injected in the side channels (blue arrows). The symmetry plane used to simplify and reduce the computational domain is highlighted in red. (**D**) Dimensions of the microfluidic chip used to reconstruct the numerical domain.

Table 2
Boundary conditions adopted in the first set of numerical simulations to study the impact of increasing total flow rate at fixed fibroin:acetone ratios on the mixing process.

	Fibroin:acetone ratio 1:3			**Fibroin:acetone ratio 1:5**		
Total flow rate (mL/min)	8	21.5	140	8	21.5	140
$v_{acetone}$ (m/s)	1.19	3.2	20.83	1.32	3.55	23.15
$v_{fibroin}$ (m/s)	0.79	2.13	13.89	0.53	1.42	9.26

$$VoC = 100 \times \frac{\sum_{i=1}^{N}\sum_{j=1}^{M}\sum_{k=1}^{L} V_{ijk0.05<X_{ijk}<0.3}}{\sum_{i=1}^{N}\sum_{j=1}^{M}\sum_{k=1}^{L} V_{ijk}}$$

where V_{ijk} corresponds to the volume of the ijk^{th} 3D cell of the microfluidic domain, where the optimal water mass fraction conditions are reached.

This variable also enabled the determination of the process efficiency (η), quantifying the fraction of the aqueous fibroin solution that is effectively exposed to acetone within the microfluidic domain:

$$\eta = 100\frac{A_{ij0.05<X_{ij}<0.3}}{A_{Outlet}}$$

where A_{Outlet} corresponds to the area of the microfluidic chip outlet, while $A_{ij0.05<X_{ij}<0.3}$ corresponds to the area of the outlet in which there is fibroin that may change configuration and then produce nanoparticles. Hence, η is pivotal for indicating whether any further SFN formation or aggregation may occur outside the microfluidic chip.

The shear rate distribution experienced by the two fluids in contact, which represents the second critical condition for proper SFN formation, was analyzed using the VoC. According to the literature (Matsumoto et al., 2008, Matthew et al., 2022a), proteins similar to fibroin required a minimum shear rate of 1000 s^{-1} to have enough mechanical work for nanoparticle formation. Nevertheless, high shear rates (*i.e.,* $>$*1000* s^{-1}) can induce gelation of the aqueous fibroin solution even without desolvation, and a sufficiently high flow rate is necessary to expel the forming hydrogel and prevent chip clogging. Finally, the residence times of hypothetical SFNs forming within the VoC were determined to assess formation dynamics.

The performed pseudo-transient simulations employed a coupled CFD-species transport framework available in the commercial solver. Velocity-pressure coupling was resolved using a coupled algorithm, with the flux equations discretized using the Rhie-Chow momentum interpolation method. The PRESTO! scheme was applied for pressure, while the second-order upwind scheme was used for momentum, diffusion, and energy equations. A residual convergence criterion of 1e^{-3} was

Table 4
Rheological parameters for 1.5% w/v fibroin in water and acetone. The densities of both fluids were obtained from the ANSYS Fluent fluid library.

	ρ (kg/m^3)	**μ (Pa•s)**	**n (−)**	**k (Pa•s^n)**
Fibroin	1000	Min: 0.001 Max: 2.1412	0.074	2.1412
Acetone	800	0.0003	–	–

Table 3
Boundary conditions adopted in the third and fourth sets of numerical simulations, as supplied by the Random Forest model.

	Fibroin:acetone ratio 1:5				**Fibroin:acetone ratio 1:10**	**Fibroin:acetone ratio 1:20**	**Fibroin:acetone ratio 1:40**
Total flow rate (mL/min)	50	60	90	100	21.5	21.5	21.5
$v_{acetone}$ (m/s)	8.27	9.92	14.88	16.53	3.88	4.06	4.16
$v_{fibroin}$ (m/s)	3.31	3.97	5.96	6.61	0.53	0.41	0.21

enforced to guarantee minimal variation between successive time steps.

All simulations were performed in *ANSYS Fluent 2025 R1* (Ansys Inc., Canonsburg, PA, USA) on a workstation equipped with a 13th Gen Intel (R) Core™ i9-13900 K (3.0 GHz) processor and 128 GB RAM.

3. Results

This study aimed to optimize the production of SFNs via controlled desolvation in a microfluidic device. Fibroin, initially in its solid Silk II conformation, was solubilized to the Silk I conformation in aqueous solution. The subsequent desolvation in acetone induced a reversion to Silk II, resulting in the precipitation of solid SFNs (Zhang et al., 2012). This desolvation process was performed within a microfluidic chip, which was fed by two independent syringe pumps: one delivering the fibroin solution and the other delivering acetone. Several batches of SFNs were prepared by varying the experimental conditions according to a DOE, focusing on two main factors: the fibroin:acetone volumetric ratio (1:5 and 1:3) and the total flow rate (8, 21.5, 35, 70, 105, and 140 mL/min), which is the combined flow rate of both pumps.

Particle size and size distribution of freshly prepared SFNs were measured using NTA. For each sample, measurements were taken from five different regions, producing five curves (one per recorded video) that relate nanoparticle concentration (particles/mL, y-axis) to particle size (x-axis), as shown in Fig. S2. Since SFN concentration varies across regions of the same sample, the curves were normalized to have equal areas under the curves, allowing meaningful comparison of peak positions. From these normalized distributions, the mode and percentile diameters were determined, as summarized in Table 5.

With the aim of developing a process that produces small nanoparticles with a homogeneous size distribution while minimizing acetone consumption, an initial descriptive phase investigated the influence of the total flow rate and the fibroin:acetone ratio. This ratio is defined both volumetrically (e.g., 1:3 or 1:5 fibroin to acetone) and as a pump flow rate ratio; optimizing this variable is key to reducing solvent use during SFN preparation. Because the particle size distribution is typically non-symmetric and right-skewed, three key response variables derived from NTA percentile diameters were analyzed to capture both central tendencies and distributional extremes: the median particle size (d_{50}), the mode, which describe the average and most frequent particle sizes, and the width of the central 60% of the size distribution (d_{80}-d_{20}) to quantify homogeneity, where a lower difference indicates a more uniform population. Therefore, while Table 5 reports the full range of percentiles (d_{10}-d_{100}), these three metrics were selected for their mechanistic relevance in defining nanoparticle size and distribution width.

Overall, results demonstrate that the fibroin:acetone ratio and total flow rate interact to influence SFN size distribution (d_{80}-d_{20}), median, and mode (Fig. 3). Fig. 3A shows the effects of the fibroin:acetone ratio and total flow rate on the spread in the particle size distribution, as determined by fitting the experimental data with a linear model. For batches prepared at total flow rates of 8, 21.5, and 105 mL/min, the size distribution remains largely unchanged as the fibroin:acetone ratio increases. Conversely, at total flow rates of 70 and 140 mL/min, the d_{80}-d_{20} decreases with increasing ratio, suggesting that higher ratios at elevated flow rates promote narrower particle size distributions, likely reflecting more efficient particle formation, improved mixing, or reduced agglomeration. Particle sizes varied widely across batches, with d_{10} values ranging from 24.5 to 176.5 nm and d_{100} values from 250.5 to 999.5 nm. Batches prepared at higher flow rates (70 or 140 mL/min) generally exhibited broader size distributions, whereas lower fibroin: acetone ratios (e.g., 1:3) at high flow rates often produced smaller d_{10} values and more compact distributions (e.g., batch 6). Higher fibroin: acetone ratios (e.g., 1:5) combined with low flow rates tended to yield larger particles (e.g., batch 15). Some variability is observed between batches prepared under nominally identical conditions, particularly at intermediate and high flow rates, and even batches prepared at the same

Table 5

Dataset of the batches prepared; d_{10}, d_{20}, …, d_{100} refer to percentile diameters (nm), indicating the particle diameter below which that percentage of the sample falls in the particle size distribution.

Batch n.	Ratio	Total flow rate (mL/min)	Mode	Total number of particles	d_{10} (nm)	d_{20} (nm)	d_{30} (nm)	d_{40} (nm)	d_{50} (nm)	d_{60} (nm)	d_{70} (nm)	d_{80} (nm)	d_{90} (nm)	d_{100} (nm)
1	5	8.0	144	42,417,745	62.5	100.5	114.5	129.5	147.5	152.5	157.5	170.5	198.5	382.5
2	5	21.5	153	1.14E + 08	128.5	139.5	150.5	161.5	172.5	187.5	210.5	231.5	252.5	493.5
3	5	35.0	181	68,811,824	117.5	135.5	153.5	173.5	190.5	218.5	241.5	262.5	345.5	650.5
4	3	8.0	199	1.94E + 08	46.5	124.5	174.5	189.5	200.5	211.5	223.5	256.5	305.5	518.5
5	3	21.5	46	3.79E + 08	42.5	44.5	47.5	49.5	58.5	74.5	107.5	176.5	280.5	999.5
6	3	35.0	25	76,717,912	24.5	34.5	47.5	60.5	89.5	107.5	120.5	133.5	143.5	250.5
7	3	8.0	163	1.97E + 08	94.5	141.5	157.5	171.5	185.5	199.5	223.5	250.5	281.5	629.5
8	5	8.0	173	92,882,361	72.5	108.5	147.5	170.5	190.5	217.5	237.5	259.5	342.5	577.5
9	3	21.5	44	3.1E + 08	43.5	52.5	108.5	123.5	136.5	194.5	213.5	223.5	236.5	488.5
10	5	21.5	163	77,388,739	119.5	141.5	157.5	169.5	184.5	221.5	240.5	312.5	353.5	541.5
11	3	35.0	136	1.49E + 08	90.5	109.5	126.5	137.5	150.5	168.5	183.5	196.5	216.5	404.5
12	5	35.0	139	66,923,850	115.5	129.5	148.5	168.5	186.5	215.5	253.5	317.5	395.5	719.5
13	3	21.5	29	2.93E + 08	28.5	34.5	46.5	56.5	66.5	90.5	112.5	126.5	149.5	256.5
14	3	8.0	145	4.76E + 08	107.5	128.5	144.5	161.5	179.5	199.5	222.5	251.5	280.5	743.5
15	5	8.0	231	2.26E + 08	176.5	199.5	215.5	229.5	241.5	254.5	276.5	306.5	338.5	597.5
16	3	21.5	136	2.46E + 08	53.5	86.5	106.5	133.5	152.5	176.5	190.5	215.5	248.5	552.5
17	3	21.5	176	3.29E + 08	129.5	151.5	167.5	182.5	198.5	214.5	232.5	254.5	292.5	799.5
18	3	35.0	176	1.94E + 08	62.5	90.5	122.5	141.5	156.5	169.5	184.5	196.5	215.5	450.5
19	5	35.0	179	2.43E + 08	97.5	127.5	142.5	169.5	182.5	189.5	199.5	220.5	251.5	445.5
20	5	8.0	194	2.34E + 08	169.5	180.5	190.5	200.5	212.5	227.5	244.5	265.5	310.5	633.5
21	5	21.5	194	2.25E + 08	153.5	169.5	181.5	193.5	203.5	217.5	232.5	260.5	291.5	661.5
22	5	35.0	169	1.95E + 08	139.5	158.5	170.5	185.5	201.5	217.5	236.5	253.5	286.5	498.5
23	3	8.0	161	1.23E + 08	139.5	151.5	162.5	175.5	188.5	205.5	222.5	241.5	270.5	431.5
24	3	21.5	196	2.61E + 08	110.5	130.5	157.5	172.5	191.5	211.5	226.5	245.5	277.5	726.5
25	3	35.0	185	2.08E + 08	121.5	138.5	161.5	175.5	185.5	195.5	208.5	227.5	286.5	485.5
26	3	70.0	136	1.74E + 08	116.5	128.5	136.5	156.5	169.5	185.5	207.5	245.5	307.5	657.5
27	3	140.0	163	1.37E + 08	150.5	159.5	173.5	194.5	221.5	242.5	273.5	343.5	382.5	860.5
28	5	70.0	142	1.14E + 08	107.5	117.5	126.5	134.5	144.5	155.5	171.5	184.5	222.5	381.5
29	5	140.0	151	94,202,505	119.5	133.5	145.5	151.5	160.5	170.5	184.5	202.5	254.5	439.5
30	3	105.0	154	76,638,056	118.5	129.5	140.5	146.5	164.5	176.5	198.5	216.5	239.5	456.5
31	5	105.0	139	2.26E + 08	119.5	129.5	148.5	165.5	178.5	189.5	206.5	227.5	268.5	530.5

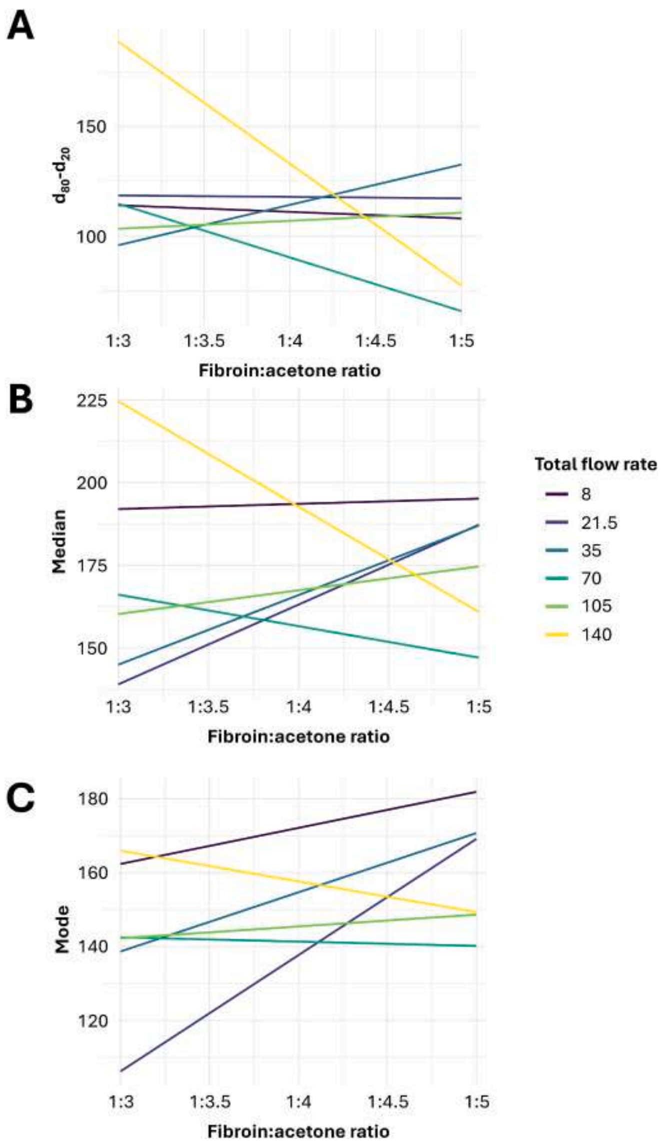

Fig. 3. Interaction plot showing the effect of fibroin:acetone ratio and total flow rate on (**A**) particle size distribution homogeneity (d_{80}-d_{20}), (**B**) the median, and (**C**) the mode. The median, mode, and d_{80}-d_{20} are reported in nm, while the total flow rate is reported in mL/min.

flow rate and ratio sometimes showed differences in size distribution. For example, among batches prepared at a 1:5 fibroin:acetone ratio and 8 mL/min flow rate, batch 1 exhibited the smallest and narrowest distribution, batch 15 produced larger particles with a peak at 231 nm, and batch 20 showed similarly large particles but with a slightly lower mode and broader distribution, indicating mixed populations. In contrast, batches prepared at a 1:5 fibroin:acetone ratio and 21.5 mL/min flow rate were more consistent; for instance, batches 2 and 10 differed mainly in their d_{100} values. This reflects the intrinsic sensitivity of microfluidic nanoprecipitation to local flow conditions, residence time, solvent exposure, and minor differences in fibroin solubilization, while environmental factors such as temperature fluctuations or minor pump differences may also contribute.

The effects of the fibroin:acetone ratio and total flow rate on the median (Fig. 3B) and mode (Fig. 3C) further highlight these trends. At a low total flow rate of 8 mL/min, the median remains largely unchanged with varying fibroin:acetone ratios, whereas at 21.5 and 35 mL/min, the median increases with higher fibroin:acetone ratios. Conversely, at 70 and 140 mL/min, the median decreases with increasing fibroin:acetone ratio. For the mode, low flow rates (8, 21.5, and 35 mL/min) show an increase with increasing fibroin:acetone ratios, while at 70 mL/min, the mode is unaffected. At 105 mL/min, only a slight increase in mode occurs with higher fibroin:acetone ratios, whereas the highest flow rate tested (140 mL/min) results in a decrease in mode as the fibroin:acetone ratio increases.

The frequent crossings and non-monotonic trends observed in Fig. 3 indicate transitions between distinct nanoparticle formation regimes, in which the relative contributions of shear rate, residence time, and solvent exposure shift with total flow rate and fibroin:acetone ratio, highlighting the system's non-linear behavior. Motivated by these observations, the second phase employed predictive modeling to systematically explore these non-linear parameter interactions and identify parameter regions associated with improved outcomes within the experimentally sampled design space, focusing on process understanding rather than defining discrete mechanistic regimes. Initially, a quadratic power model was fitted to generate response surfaces relating the input parameters to the outcomes (d_{80}-d_{20} and median), as shown in Fig. S3. However, these surfaces mainly appeared flat, with an extended central region where the effects of varying operational parameters on size and size homogeneity were not clearly distinguishable. To address this, a Random Forest model was trained to predict d_{80}-d_{20}, median, and mode. This nonparametric regression approach, based on an ensemble of decision trees trained on random subsets of the data, captures non-linear trends between process parameters (flow ratio and total flow rate) and distribution-level descriptors, rather than locating extrema or resolving fine surface geometry (Parmar et al., 2019, Schonlau and Zou, 2020). Accordingly, Random Forest predictions were interpreted only within the bounds of the experimental domain and used to inform parameter exploration rather than extrapolation to untested conditions.

Fig. 4A (and supplementary File F1) shows the surface predicting d_{80}-d_{20} as a function of the fibroin:acetone ratio and total flow rate. The surface shows that d_{80}-d_{20} increases nonlinearly with both the fibroin:acetone ratio and the total flow rate, suggesting a strong interaction between the two. Specifically, the surface slope is upward as the total flow rate increases and the fibroin:acetone ratio decreases, indicating that operating at lower fibroin:acetone ratios and higher total flow rates yields larger d_{80}-d_{20} values, indicative of reduced particle-size homogeneity. Conversely, the surface exhibits a localized downward slope, primarily in the lower-to-mid range of total flow rate and at relatively higher fibroin:acetone ratios (approximately 1:3.5 to 1:4). These regions indicate parameter ranges associated with more uniform particle size distributions. In particular, total flow rates between 60 and 90 mL/min and fibroin:acetone ratios ranging from 1:5 to 1:4 are associated with minimized d_{80}-d_{20}. However, this region is narrow, and even minor changes in a single parameter can push the system out of the ideal range, increasing d_{80}-d_{20} and thus decreasing nanoparticle homogeneity, which highlights the intrinsic sensitivity of SFN formation to coupled hydrodynamic and solvent-exchange parameters and defines a limited but actionable design space for achieving high particle-size homogeneity.

Similarly, predictive surfaces for the median (Fig. 4B, supplementary File F2) and the mode (Fig. 4C, supplementary File F3) were obtained. Regarding the median (Fig. 4B), the surface clearly slopes upward at total flow rates between 140 and 125 mL/min and 1:3 fibroin:acetone ratios, reaching a median of approximately 220 nm. The surface then slopes downward for total flow rates between 120 and 90 mL/min and fibroin:acetone ratios of 1:5 or 1:4. The surface reveals two distinct valley regions where the downward slope reaches its minimum: the first region occurs at a fibroin:acetone ratio of 1:5 and total flow rates ranging from 50 to 85 mL/min, with the lowest point at 70 mL/min and a corresponding median value of 143 nm; the second valley also occurs at a 1:5 fibroin:acetone ratio, between 21.5 and 10 mL/min, reaching its minimum at 15 mL/min flow with a corresponding median value of 144 nm. Between these two valleys, at total flow rates ranging from 25 to 50 mL/min with the same 1:5 fibroin:acetone ratio, the surface rises, with

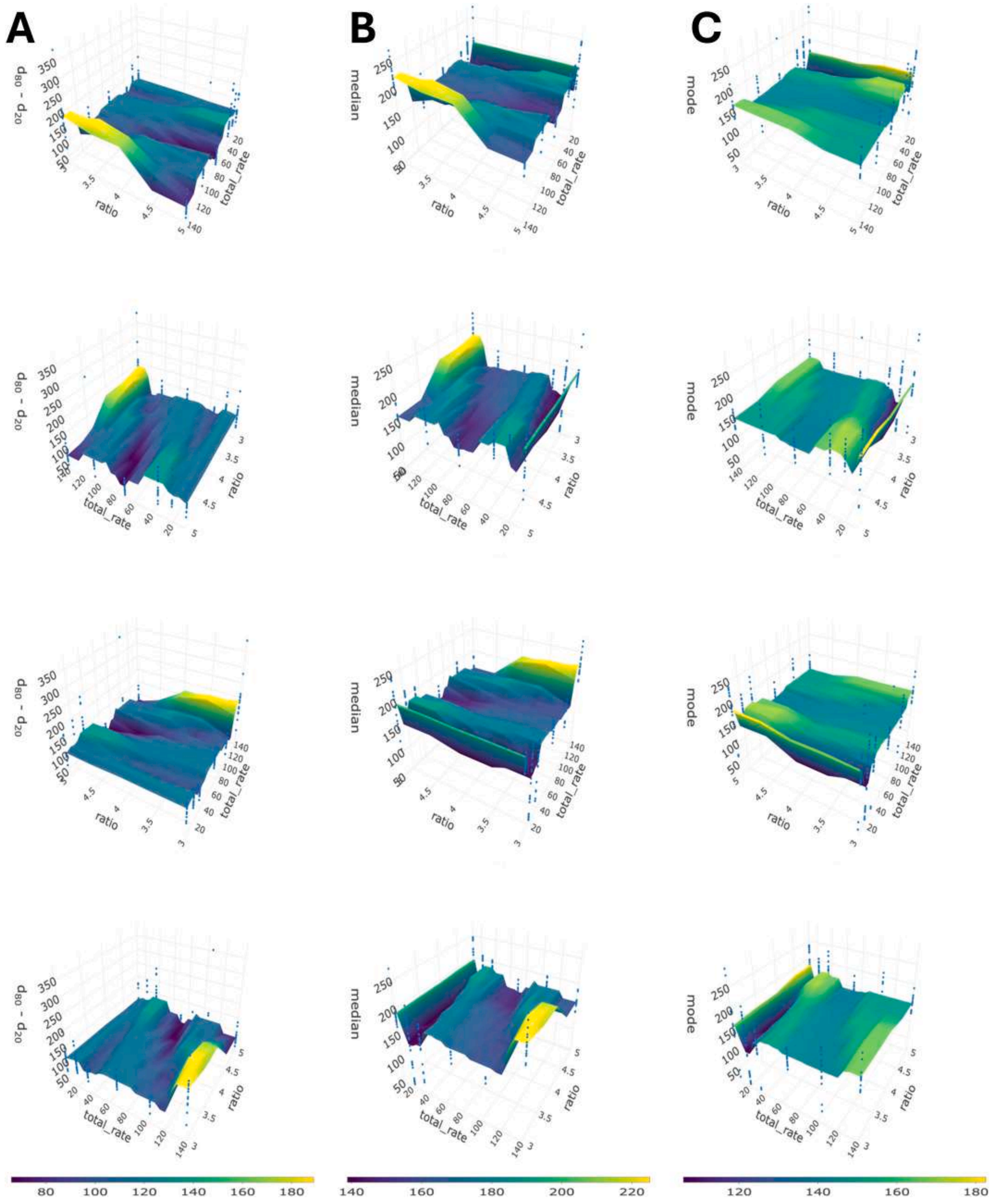

Fig. 4. Surface generated by a Random Forest model that pictures particle size distribution homogeneity (d_{80}-d_{20}) (**A**), the median (**B**), and mode (**C**) as a function of the fibroin:acetone ratio (ratio) and total flow rate (total_rate). Blue points represent the experimental data, while the interpolated surface illustrates the underlying trend. The d_{80}-d_{20} are reported in nm, while the total flow rate is reported in mL/min.

median values ranging from 173 to 186 nm, indicating an increase in particle size in this transitional region. Regarding the mode (Fig. 4C), the generated surface appears flat overall, with fewer pronounced upward and downward slopes. The most prominent upward region occurs at a total flow rate of 8 mL/min and a 1:5 fibroin:acetone ratio, with a mode at 188 nm (the highest point on the surface). The surface then slopes down, forming a moderate valley region at the total flow rate of 15 mL/min and a 1:5 fibroin:acetone ratio, with a mode value of 140 nm. The only well-defined valley occurs between 20 and 25 mL/min of total flow rate and at a 1:3 fibroin:acetone ratio, where the mode reaches its minimum at approximately 107 nm. Following this low point, the surface slopes upward again, reaching a maximum value of 150 nm at a total flow rate of 60 mL/min for both 1:3 and 1:5 fibroin:acetone ratios, and remains relatively stable up to 140 mL/min.

SEM analysis revealed that SFNs exhibit a predominantly spherical morphology with smooth, well-defined surfaces, regardless of the total flow rate or the fibroin:acetone ratio (Fig. 5). Occasional particle clusters are observed; these aggregates are mainly attributed to sample-preparation artifacts associated with freeze-drying, which can locally concentrate nanoparticles and promote apparent agglomeration, as widely reported in SFN characterization by SEM and transmission electron microscopy (Montalban et al., 2018, Rahmani et al., 2019, Zhao

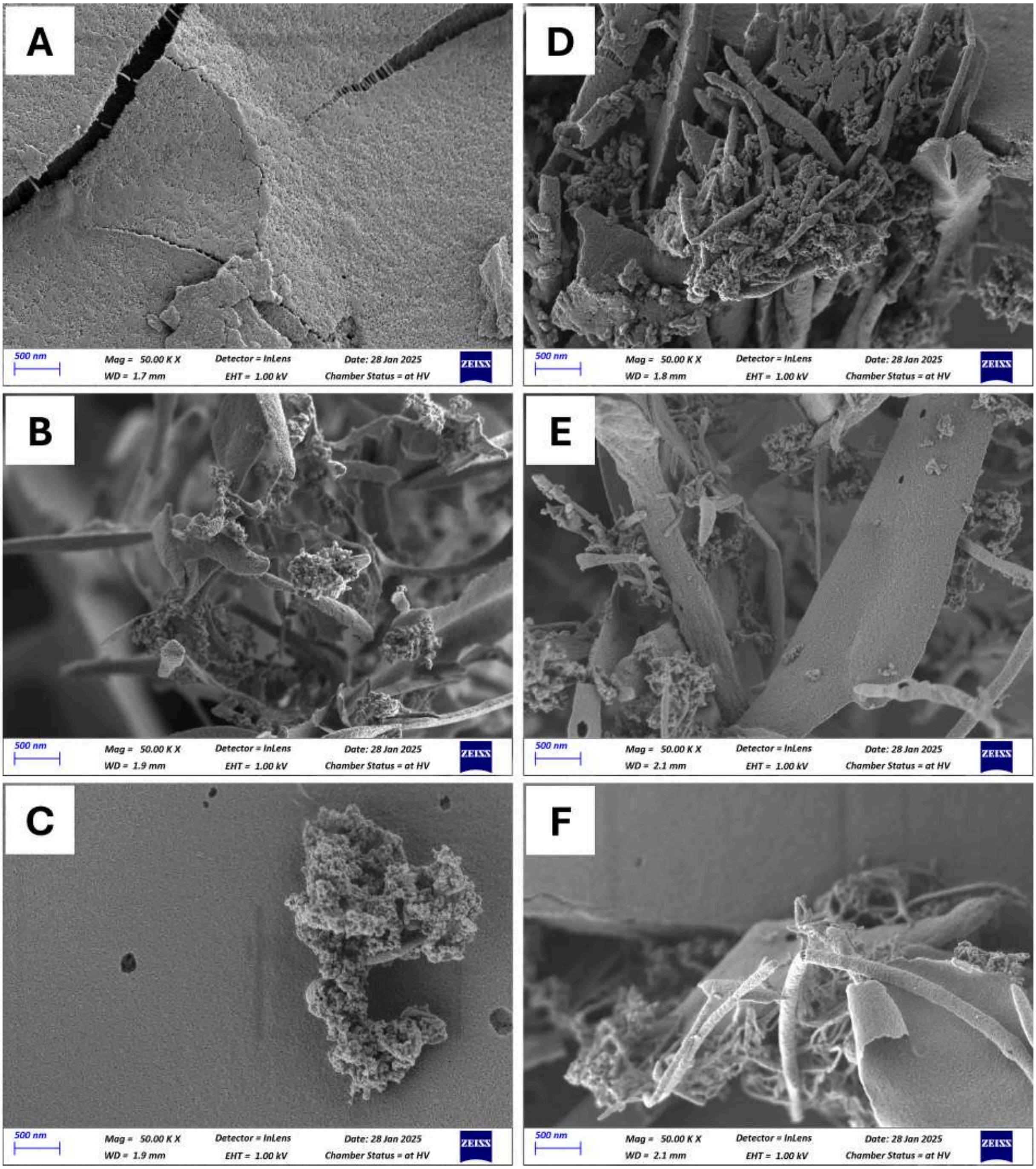

Fig. 5. Representative SEM images show SFNs obtained at varying fibroin:acetone volumetric ratios and total flow rates: (**A**) fibroin:acetone ratio 1:5, total flow rate 8 mL/min; (**B**) fibroin:acetone ratio 1:5, total flow rate 21.5 mL/min; (**C**) fibroin:acetone ratio 1:5, total flow rate 35 mL/min; (**D**) fibroin:acetone ratio 1:3, total flow rate 8 mL/min; (**E**) fibroin:acetone ratio 1:3, total flow rate 21.5 mL/min; and (**F**) fibroin:acetone ratio 1:3, total flow rate 35 mL/min. All images were acquired at 50 k×.

et al., 2014, Lozano-Perez et al., 2017). Importantly, no marked morphological differences are detected as a function of flow rate or fibroin:acetone ratio, supporting the conclusion that variations in hydrodynamic conditions primarily affect particle size distribution rather than particle shape. Accordingly, CFD-derived metrics were interpreted in relation to size distribution and formation efficiency rather than particle morphology, which remained invariant across the explored parameter space.

CFD results show that increases in both the total flow rate and the fibroin:acetone ratio alter the velocity profiles and the downstream redistribution of the VoC (Fig. 6). In more detail, the total flow rate directly affects the velocities within the microfluidic channel, leading to

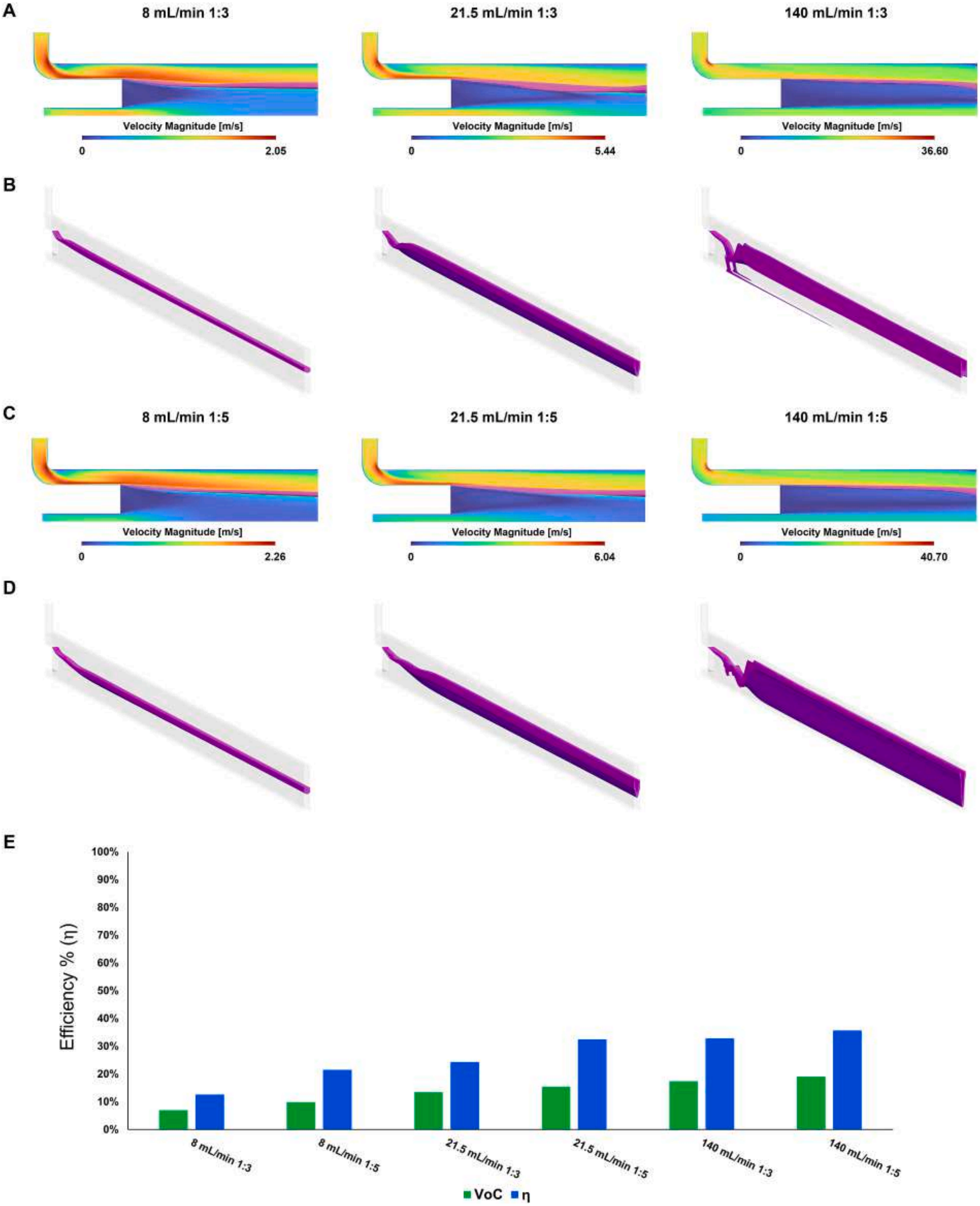

Fig. 6. (**A**) Velocity profiles with overlapped VoC (purple) at a fibroin:acetone ratio of 1:3 and increasing the total flow rate at the microfluidic chip inlet section; (**B**) topology of VoC along the channels under the same conditions. (**C**) Velocity profiles with overlapped VoC at a fibroin:acetone ratio of 1:5 and increasing the total flow rate at the microfluidic chip inlet section; (**D**) topology of VoC along the channels under the same conditions. (**E**) Histogram showing the VoC and the process efficiency % (η) for each investigated boundary condition.

pronounced flow separation at the inlet, especially at higher total flow rates (Fig. 6A and 6C). Therefore, an increased total flow rate may lead to two effects: (i) a reduction in residence time due to higher velocities; and (ii) accumulation of unreacted material in the initial section due to a bigger zone at low velocities where flow separation takes place, which can promote clogging. At the same time, higher velocities can help mitigate this risk by facilitating the detachment of gelated fibroin. Reynolds numbers for each condition were then calculated using the average velocity under Poiseuille flow assumptions. However, the channel features a rectangular cross-section, which yields lower velocities due to the larger area for a given hydraulic diameter. Interestingly, the VoC topology was markedly altered by fluid-dynamic conditions (Fig. 6B and 6D). These variations led to changes in system efficiency: increasing the total flow rate led to a modest rise in VoC, whereas increasing the fibroin:acetone ratio improved system efficiency, suggesting that further increases in the ratio may further enhance η and ultimately yield higher SFN production (Fig. 6E). Indeed, enhancing efficiency is essential to ensure that nanoparticle formation, or, in the

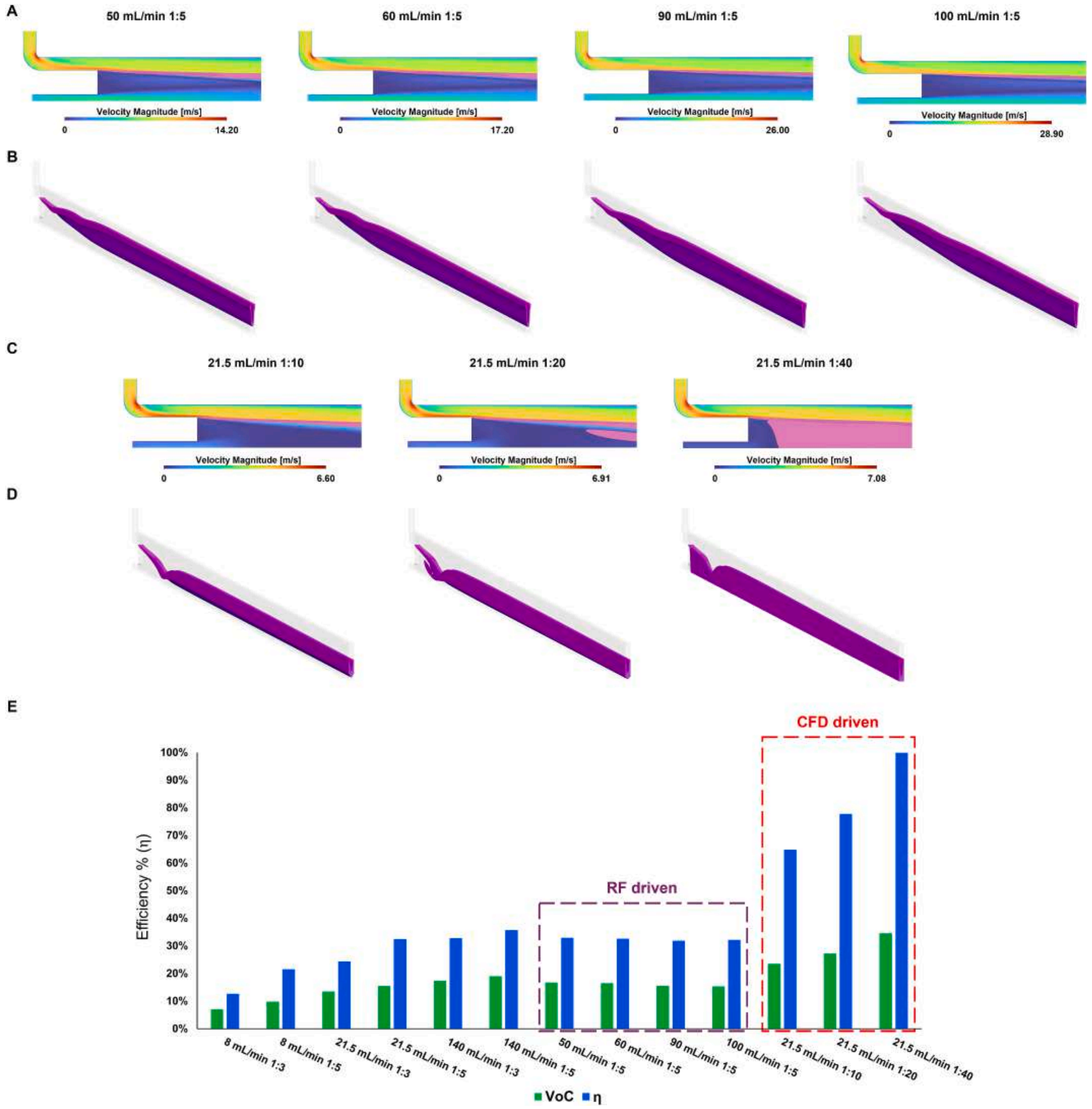

Fig. 7. (**A**) Velocity profiles with overlapped VoC (purple) in the microfluidic chip inlet section at fixed fibroin:acetone ratio and increasing total flow rate values selected by the Random Forest model; (**B**) corresponding VoC topology along the channels at the same conditions. (**C**) Velocity profiles with overlapped VoC (red) in the microfluidic chip inlet section at fixed total flow rate and increasing fibroin:acetone ratio values selected for maximizing η; (**D**) corresponding VoC topology along the channels under the same conditions. (**E**) Histogram showing the VoC and the process efficiency % (η) for each investigated boundary condition; the CFD-driven selection is highlighted in red and the Random Forest selection is highlighted in purple.

worst case, aggregation, occurs within the microfluidic channel rather than in the collection vessel.

Shear rates were evaluated both within the VoC and in the unreacted portion of the fibroin solution to determine whether they exceeded the critical threshold. In both volumes, nearly 100% of the control volumes exhibited shear rates above this critical value, indicating that conditions within the VoC are optimal for SFN formation. However, elevated shear rates were also observed in unreacted regions, suggesting that gelation may occur concurrently. A second and third set of numerical simulation were then performed to determine if any enhancement of the SFN manufacturing process can be obtained using two approaches: (i) adopting the boundary conditions given by the Random Forest model (Fig. 7A and 7B) and (ii) using the flow rate ratio as parameter to increase dilution rate, since its effect on the η is highlighted on the first set of simulation (Fig. 7C and 7D). The Random Forest-based numerical simulations showed fluid separation zones (Fig. 7A), VoC distribution, and η (Fig. 7B), similar to the results observed between 21.5 and 140 mL/min. This is mainly due to the Random Forest model's inability to predict working conditions outside the boundaries used to train the mathematical model.

While considering the numerically informed boundary conditions, the fluid separation zone was reduced (Fig. 7C), and the VoC increased, following the flow rate ratio trend (Fig. 7D). The increase in the fibroin: acetone ratio at 21.5 mL/min allows increasing η to 100% and also increasing VoC (Fig. 7E).

4. Discussion

This study systematically optimized the microfluidic desolvation of soluble silk fibroin into solid SFNs by varying the fibroin:acetone ratio (1:3–1:5) and the total flow rate (8–140 mL/min). Nanoparticle size and distribution were quantified through NTA and interpreted using statistical and Random Forest models, while complementary CFD simulations were used to provide a mechanistic interpretation of how flow rate, mixing dynamics, residence time, local shear rate, and solvent-rich volume fractions jointly influence SFN formation. Importantly, the key contribution of this work is not merely the fabrication of microfluidic SFNs – which has been previously reported – but the development of a mechanistically informed, data-guided approach for interpreting microfluidic nanoprecipitation behaviour. While the quantitative applicability of the models is currently limited to the specific device geometry explored, this work illustrates a transferable workflow by demonstrating how solvent ratios and transport phenomena shape experimentally observed nanoparticle outcomes. By coupling machine learning with CFD-derived physical descriptors, operating regions associated with favourable nanoparticle characteristics can be rationalized post hoc rather than identified solely through empirical trial-and-error. From a pharmaceutical manufacturing perspective, this strategy supports hypothesis-driven process understanding and provides a foundation for future Quality-by-Design implementation, rather than constituting predictive process control at this stage.

Random Forest analysis highlighted strong, non-linear dependencies of SFN median size, mode and distribution width (d_{80}-d_{20}) on both total flow rate and the fibroin:acetone ratio, with experimentally favourable homogeneity confined to narrow operating regions at intermediate flow rates (60–90 mL/min) and higher fibroin:acetone ratios (1:4 or 1:5). In this context, percentile-based metrics capture the differential response of nanoparticle subpopulations to hydrodynamic and solvent-exchange conditions, providing insight into distribution broadening and aggregation phenomena that would be obscured by mean size or polydispersity index alone. The presence of multiple competing formation regimes explains why linear and quadratic models were insufficient to describe the data and why a Random Forest approach was required to resolve the non-linear interactions observed experimentally. CFD simulations mechanistically rationalize the model-identified trends, providing a physical interpretation of velocity profiles, residence time, and the VoC within the microfluidic channel. Increasing acetone fractions expands the VoC, thereby increasing the fraction of fibroin exposed to conditions conducive to desolvation and enhancing η. Shear-rate analysis shows that, within the experimentally favourable operating region, the VoC consistently exceeds the critical shear threshold required for efficient SFN formation, supporting a mechanistic interpretation of the operating region highlighted by the Random Forest model. Collectively, these results demonstrate that nanoparticle homogeneity emerges from synchronized nucleation and growth under well-defined hydrodynamic and solvent-exchange conditions, rather than from any single parameter acting in isolation. Intermediate flow rates balance solvent diffusion-driven desolvation with shear-induced fibroin chain alignment, whereas excessively low flow rates favor aggregation due to prolonged residence time, and excessively high flow rates promote heterogeneous growth due to insufficient residence time and non-uniform solvent exposure. While increasing total flow rate enhances shear and mixing, excessively high rates reduce residence time, preventing uniform fibroin desolvation and β-sheet formation. Consequently, optimal nanoparticle homogeneity arises at intermediate flow rates, where mixing efficiency and residence time are balanced, whereas very high flow rates may cause reagents to exit the channel before complete nanoprecipitation occurs.

Mechanistically, the coupled effects of flow rate and solvent ratio regulate the local solvent environment, triggering fibroin desolvation and the Silk I → Silk II conformational transition, ultimately defining nanoparticle structural uniformity. CFD analysis indicates that spatial solvent heterogeneity determines whether fibroin chains undergo uniform β-sheet nucleation or experience localized gelation, reinforcing the necessity of homogeneous solvent exposure. These observations are consistent with established knowledge of silk fibroin self-assembly: fibroin in aqueous solution predominantly adopts the Silk I conformation with low β-sheet content (Asakura, 2021), while exposure to organic solvents such as acetone promotes β-sheet formation (Nam and Park, 2001). The initial conformational transition increases solution viscosity and predisposes the system to gelation if solvent exposure is insufficiently rapid or homogeneous. Effective nanoprecipitation occurs only when β-sheet conversion is both extensive and spatially uniform. Accordingly, homogeneous SFN formation is favored at lower fibroin fractions (30–10%), where higher acetone content suppresses gelation and enables uniform precipitation throughout the flow field. These mechanistic principles are consistent with broader perspectives on silk protein self-assembly, in which solvent environment and conformational transitions govern material behavior (Matthew and Seib, 2023). Consistent with this molecular picture, microfluidic nanoprecipitation studies – including the present work – show that a minimum fibroin: acetone ratio of 1:3 is required for SFN formation; below this threshold, no nanoparticles are detected despite local gelation or partial precipitation (Ferrera et al., 2024). The experimentally favourable operating region identified at higher acetone fractions (1:4 or 1:5) is therefore mechanistically justified, as elevated acetone levels ensure rapid, spatially homogeneous desolvation and controlled β-sheet nucleation under the residence-time and shear regime imposed by intermediate flow rates. Prior studies have similarly demonstrated that exceeding critical shear threshold can induce shear-driven assembly that counteracts supersaturation-driven nanoprecipitation, whereas intermediate shears promote uniform, spherical nanoparticles (Matthew et al., 2022a). Scale-up studies further emphasize that preserving mixing time and shear regime during volumetric scaling is essential to maintain nanoparticle size distribution and crystallinity (Mansor et al., 2025).

Beyond silk fibroin, the mechanistic principles identified in this study – such as the interplay between solvent exposure, shear, and residence time – may guide hypothesis generation and inform experimental design in other protein- or polymer-based nanoprecipitation systems with similar transport constraints. While quantitative outcomes remain specific to the device geometry and silk-acetone system studied here, the framework enables researchers to move away from purely empirical parameter screening by clarifying how transport phenomena govern particle nucleation and growth (Solomun et al., 2020). Such mechanistic understanding is critical for pharmaceutical translation: achieving precise control over nanoparticle size distribution and structural uniformity has direct structure-performance implications, including predictable cellular uptake, improved colloidal stability, and reduced aggregation propensity (Kundu et al., 2010, Wang et al., 2015, Moore et al., 2015). By improving batch-to-batch reproducibility, this data-guided approach contributes to meeting the quality requirements necessary for clinical applications. However, achieving high structural uniformity introduces a critical trade-off regarding the study's initial sustainability objectives. While it was hypothesized that microfluidic optimization might permit a reduction in solvent consumption, both the experimental observations and Random Forest trend analysis converge on the opposite conclusion: the most homogeneous SFNs arise only at higher acetone fractions (1:4 or 1:5). Mechanistically, these higher fractions are required to suppress gelation-driven heterogeneity and ensure uniform β-sheet conversion under the residence-time and shear regimes found at intermediate flow rates.

Ultimately, while microfluidics enhances reproducibility and scalability – the identified operating conditions can be translated to multichannel or modular chip architectures, enabling high-throughput production of SFNs without compromising particle uniformity or consistency (Lin et al., 2023, Matthew et al., 2022b, Gimondi et al., 2023) – it does not inherently reduce solvent demand in this system, yet it enables an evidence-based evaluation of the trade-off between solvent usage and nanoparticle quality, which is critical for rational pharmaceutical process development.

5. Conclusions

The combination of Random Forest predictive modeling and CFD provides a mechanistically informed approach for interpreting SFN formation in the Fluidic 640 microfluidic device. This workflow highlighted experimentally favourable operating regions associated with more uniform particle size and higher process efficiency, including intermediate flow rates (60–90 mL/min) and higher fibroin:acetone ratios (1:4 or 1:5). By integrating model-derived insights with mechanistic understanding of flow, mixing, and residence time, the approach facilitates structured interpretation of process trends and supports hypothesis-driven exploration, reducing reliance on purely empirical trial-and-error experimentation. Although the quantitative findings are specific to the device and parameter space studied here, the study provides mechanistic insights into the interplay of shear, solvent exposure, and residence time, which may inform the design and analysis of similar microfluidic nanoprecipitation experiments and provide a foundation for future data-guided process development.

CRediT authorship contribution statement

Edoardo Bertania: Writing – review & editing, Methodology, Investigation. **Angelo Modena:** Writing – review & editing, Methodology, Investigation. **Alessandro Caimi:** Writing – review & editing, Validation, Software, Methodology, Investigation. **Marco Bellotti:** Writing – review & editing, Validation, Software, Methodology, Investigation. **Luca Romizi:** Software. **Maurizio Rinaldi:** Writing – review & editing, Visualization, Software, Formal analysis, Data curation. **Ivana Miletto:** Methodology, Investigation. **Elia Bari:** Writing – original draft, Visualization, Supervision, Resources, Project administration, Methodology, Investigation, Funding acquisition. **Lorena Segale:** Writing – review & editing, Investigation. **Giada Diana:** Investigation. **Alessandro Candiani:** Investigation. **Maria Luisa Torre:** Writing – review & editing, Supervision, Conceptualization. **Ferdinando Auricchio:** Supervision, Conceptualization.

Funding

This work is part of the project RESALE, which has received funding from the European Commission – NextGeneration EU and Compagnia di San Paolo.

Declaration of competing interest

The authors declare the following financial interests/personal relationships which may be considered as potential competing interests: Maria Luisa Torre is the co-founder and owner of PharmaExceed s.r.l. The company had no role in the design of the experiments, data collection and analysis, decision to publish, or preparation of the manuscript.

Appendix A. Supplementary data

Supplementary data to this article can be found online at https://doi.org/10.1016/j.ijpharm.2026.126727.

Data availability

Data will be made available on request.

References

Asakura, T., 2021. Structure of Silk I (Bombyx mori Silk Fibroin before Spinning) -Type II β-Turn, Not α-Helix-. Molecules 26, 3706.

Bari, E., Perteghella, S. & Torre, M.L., 2020. Silk-based drug delivery systems, Royal Society of Chemistry.

Bari, E., Serra, M., Paolillo, M., Bernardi, E., Tengattini, S., Piccinini, F., Lanni, C., Sorlini, M., Bisbano, G., Calleri, E., Torre, M.L., Perteghella, S., 2021. Silk fibroin nanoparticle functionalization with Arg-Gly-Asp cyclopentapeptide promotes active targeting for tumor site-specific delivery. Cancers 13.

Bari, E., Ferrera, F., Altosole, T., Perteghella, S., Mauri, P., Rossi, R., Passignani, G., Mastracci, L., Galati, M., Astone, G.I., Mastrogiacomo, M., Castagnola, P., Fenoglio, D., di Silvestre, D., Torre, M.L., Filaci, G., 2023. Trojan-horse silk fibroin nanocarriers loaded with a re-call antigen to redirect immunity against cancer. J. Immunother. Cancer 11.

Bayraktar, O., Oder, G., Erdem, C., Kose, M., Cheaburu-Yilmaz, C., 2023. Selective encapsulation of the polyphenols on silk fibroin nanoparticles: optimization approaches. Int. J. Mol. Sci. 24.

Bellotti, M., Chiesa, E., Conti, B., Genta, I., Conti, M., Auricchio, F., Caimi, A., 2024. Computational-aided approach for the optimization of microfluidic-based nanoparticles manufacturing process. Ann. Biomed. Eng. 52, 3240–3252.

Ferrera, F., Resaz, R., Bari, E., Fenoglio, D., Mastracci, L., Miletto, I., Modena, A., Perteghella, S., Sorlini, M., Segale, L., Filaci, G., Torre, M.L., Giovannelli, L., 2024. Silk fibroin nanoparticles for locoregional cancer therapy: preliminary biodistribution in a murine model and microfluidic GMP-like production. Int. J. Biol. Macromol. 282, 137121.

Giglio, A., Bellotti, M., Conti, B., E-Hasnat, N., Auricchio, F., Genta, I., Caimi, A., Chiesa, E., 2024. Experimental and numerical integrated strategy for the optimization of microfluidic parameters for eudragit L100 nanoparticles and microparticles. Mol. Pharm. 21, 5842–5853.

Gimondi, S., Ferreira, H., Reis, R., Neves, N., 2023. Microfluidic devices: a tool for nanoparticle synthesis and performance evaluation. ACS Nano 17, 14205–14228.

Kong, N., 2021. Self-assembly of bombyx mori silk fibroin. Methods Mol. Biol. 2347, 69–82.

Kuhn, M., 2008. Building predictive models in R using the caret package. J. Stat. Softw. 28, 1–26.

Kundu, J., Chung, Y.-I., Kim, Y.H., Taeb, G., Kundu, S.C., 2010. Silk fibroin nanoparticles for cellular uptake and control release. Int. J. Pharm. 388, 242–250.

Lammel, A.S., Hu, X., Park, S.-H., Kaplan, D.L., Scheibel, T.R., 2010. Controlling silk fibroin particle features for drug delivery. Biomaterials 31.

Lin, H., Leng, J., Fan, P., Xu, Z., Ruan, G., 2023. Scalable production of microscopic particles for biological delivery. Mater. Adv. 4, 2885–2908.

Lozano-Perez, A.A., Rivero, H.C., Hernandez, M.D.P., Pagan, A., Montalban, M.G., Villora, G., Cenis, J.L., 2017. Silk fibroin nanoparticles: Efficient vehicles for the natural antioxidant quercetin. Int. J. Pharm. 518, 11–19.

Mansor, M., Gao, Z., Howard, F., Macinnes, J., Zhao, X., Muthana, M., 2025. Efficient and rapid microfluidics production of bio-inspired nanoparticles derived from bombyx mori silkworm for enhanced breast cancer treatment. Pharmaceutics 17.

Matsumoto, A., Lindsay, A., Abedian, B., Kaplan, D.L., 2008. Silk Fibroin solution properties related to assembly and structure. Macromol. Biosci. 8.

Matthew, S., Seib, F., 2023. Silk bioconjugates: from chemistry and concept to application. ACS Biomater Sci. Eng. 10, 12–28.

Matthew, S., Totten, J., Phuagkhaopong, S., Egan, G., Witte, K., Perrie, Y., Seib, F., 2020. Silk nanoparticle manufacture in semi-batch format. ACS Biomater Sci. Eng. 6, 6748–6759.

Matthew, S., Rezwan, R., Kaewchuchuen, J., Perrie, Y., Seib, F., 2022a. Mixing and flow-induced nanoprecipitation for morphology control of silk fibroin self-assembly. RSC Adv. 12, 7357–7373.

Matthew, S., Rezwan, R., Perrie, Y., Seib, F., 2022b. Volumetric scalability of microfluidic and semi-batch silk nanoprecipitation methods. Molecules 27.

Montalban, M.G., Coburn, J.M., Lozano-Perez, A.A., Cenis, J.L., Villora, G., Kaplan, D.L., 2018. Production of curcumin-loaded silk fibroin nanoparticles for cancer therapy. Nanomaterials 8.

Moore, T., Rodriguez-Lorenzo, L., Hirsch, V., Balog, S., Urban, D., Jud, C., Rothen-Rutishauser, B., Lattuada, M., Petri-Fink, A., 2015. Nanoparticle colloidal stability in cell culture media and impact on cellular interactions. Chem. Soc. Rev. 44, 6287–6305.

Nam, J., Park, Y., 2001. Morphology of regenerated silk fibroin: Effects of freezing temperature, alcohol addition, and molecular weight. J. Appl. Polym. Sci. 81, 3008–3021.

Pacheco, M., Eccles, L., Davies, N., Armada, J., Cakley, A., Kadambi, I., Stoppel, W., 2022. Progress in silk and silk fiber-inspired polymeric nanomaterials for drug delivery. Front. Chem. Eng. 4.

Parmar, A., Katariya, R., Patel, V., 2018. A review on random forest: An ensemble classifier. In: International conference on intelligent data communication technologies and internet of things. Springer International Publishing, Cham, pp. 758–763.

Pham, D., Tiyaboonchai, W., 2020. Fibroin nanoparticles: a promising drug delivery system. Drug Deliv. 27, 431–448.

Pinho, F., Oliveira, P., Miranda, J., 2003. Pressure losses in the laminar flow of shear-thinning power-law fluids across a sudden axisymmetric expansion. Int. J. Heat Fluid Flow 24, 747–761.

Pirota, V., Bisbano, G., Serra, M., Torre, M.L., Doria, F., Bari, E., Paolillo, M., 2023. cRGD-functionalized silk fibroin nanoparticles: a strategy for cancer treatment with a potent unselective naphthalene diimide derivative. Cancers 15, 1725.

R: The R Project for Statistical Computing https://www.r-project.org/ [Online]. [Accessed 2024-10- 17].

Rahmani, H., Fattahi, A., Sadrjavadi, K., Khaledian, S., Shokoohinia, Y., 2019. Preparation and characterization of silk fibroin nanoparticles as a potential drug delivery system for 5-fluorouracil. Adv. Pharm. Bull. 9, 601–608.

Roblin, N., Debari, M., Shefter, S., Iizuka, E., Abbott, R., 2023. Development of a more environmentally friendly silk fibroin scaffold for soft tissue applications. J. Funct. Biomater. 14.

Sánchez-Trasviña, C., Lorenzo-Anota, H., Escobar-Fernández, A., Lezama-Aguilar, D., Morales-Martínez, A., Vélez-Barceló, A., Benavides, J., Lozano, O., Rito-Palomares, M., Mayolo-Deloisa, K., 2024. Silk fibroin nanoparticles as a drug delivery system of 3,3′-diindolylmethane with potential antiobesogenic activity. ACS Omega 9, 47661–47671.

Schonlau, M., Zou, R., 2020. The random forest algorithm for statistical learning. Stata J. 20, 3–29.

Solomun, J., Totten, J., Wongpinyochit, T., Florence, A., Seib, F., 2020. Manual versus microfluidic-assisted nanoparticle manufacture: impact of silk fibroin stock on nanoparticle characteristics. ACS Biomater Sci. Eng. 6, 2796–2804.

Wang, S., Xu, T., Yang, Y., Shao, Z., 2015. Colloidal stability of silk fibroin nanoparticles coated with cationic polymer for effective drug delivery. ACS Appl. Mater. Interfaces 7, 21254–21262.

Wani, S., Zargar, M., Masoodi, M., Alshehri, S., Alam, P., Ghoneim, M., Alshlowi, A., Shivakumar, H., Ali, M., Shakeel, F., 2022. Silk fibroin as an efficient biomaterial for drug delivery, gene therapy, and wound healing. Int. J. Mol. Sci. 23.

Wongpinyochit, T., Totten, J., Johnston, B., Seib, F., 2019. Microfluidic-assisted silk nanoparticle tuning. Nanoscale Adv. 1, 873–883.

Yadav, R., Kenchegowda, M., Angolkar, M., Meghana, T., Osmani, R., Palaksha, S., Gangadharappa, H., 2024. A review of silk fibroin-based drug delivery systems and their applications. Eur. Polym. J. 216.

Zhang, H., Li, L., Dai, F., Zhang, H., Ni, B., Zhou, W., Yang, X., Wu, Y., 2012. Preparation and characterization of silk fibroin as a biomaterial with potential for drug delivery. J. Transl. Med. 10.

Zhao, Z., Li, Y., Zhang, Y., Chen, A., Li, G., Zhang, J., Xie, M., 2014. Development of silk fibroin modified poly(L-lactide)-poly(ethylene glycol)-poly(L-lactide) nanoparticles in supercritical CO2. Powder Technol. 268, 118–125.

Zhao, Z., Li, Y., Xie, M.B., 2015. Silk fibroin-based nanoparticles for drug delivery. Int. J. Mol. Sci. 16, 4880–4903.